

Probe diagnostics of high pressure microwave discharge in helium

M. R. Talukder, D. Korzec,^{a)} and M. Kando^{b)}

Graduate School of Electronic Science and Technology, Shizuoka University, 3-5-1 Johoku, Hamamatsu 432-8011, Japan

(Received 4 September 2001; accepted for publication 21 March 2002)

A method for the determination of electron temperature and plasma density in high pressure helium plasmas is established using numerical results of the continuum probe model by Cohen [Phys. Fluids **6**, 1492 (1963)]. Simple algebraic functions are derived to approximate the probe characteristics of high pressure plasmas calculated by Cohen and are applied to use iterative procedures for the determination of plasma parameters. The proposed fitting technique has allowed one to obtain reasonable plasma parameters even for the probe characteristics strongly affected by large secondary electron emission currents from the probe. Fitting of the ion saturation current may possibly be used to estimate the ion temperature, provided that the electron temperature and plasma density are known. Finally high pressure helium microwave discharges have been produced by moderate microwave power of 400 W and investigated by the present method. © 2002 American Institute of Physics. [DOI: 10.1063/1.1478801]

I. INTRODUCTION

High pressure microwave excited nonthermal plasmas are of increasing interest for reactive plasma processing¹⁻⁵ because the gas flow rate can be reduced, power transfer to plasmas becomes more effective, and contamination from the electrode and chamber wall is suppressed. Moreover, it enables one to produce a large amount of reactive species like ions, excited atoms, and free radicals. Therefore high pressure discharges have been applied to UV light sources, gas discharge lasers, and ozone production for water or air purification.⁵

For plasma source design and discharge performance optimization, sufficient knowledge of plasma parameters and their spatiotemporal behaviors are required. The Langmuir probe is a most commonly used diagnostic tool to determine the plasma parameters because it can provide local plasma properties which are difficult to determine by other diagnostic techniques. In order to analyze the measured probe characteristics under certain experimental conditions, it is important to establish a proper theoretical model, which permits one to provide reliable plasma parameters.

Several theoretical models of collisional plasmas⁶⁻¹³ have been investigated for probe diagnostics. Zakrzewski *et al.*¹¹ considered the condition that $D_\lambda \leq 3$, where R_p , λ_D , and $D_\lambda = R_p/\lambda_D$ are the probe radius, Debye length, and Debye ratio, respectively. This theory is restricted only to a few collisions in the sheath. Schulz *et al.*¹² derived a model for positive ion saturation current by taking the directed current at the sheath edge into account. They considered different conditions of collisions in the sheath, from no collision to many collisions in the pressure range up to 8 Torr. They found that at pressures up to 6 Torr, the measured ion cur-

rents were about two times larger than those predicted by their theory. This discrepancy has been attributed to the electrons emitted from the probe surface due to the interaction with the metastable atoms.

Zakharova *et al.*,⁹ Boyd,¹³ and Kagan *et al.*¹⁴ mentioned the effect of electron emission from the probe induced by the interaction with the positive ions, metastable atoms, and photons, which can lead to an overestimation of the ion current at negative probe potentials. Zakharova *et al.*⁹ presented an approximate model in the pressure range up to 20 Torr. Under their investigated conditions, they found that the effect of secondary electron emission due to metastable atoms on the probe current was not significant because of low metastable atom density around 10^{12} cm^{-3} . The effect of photocurrent on the probe current under their experimental conditions was insignificant because the excited atom density and the photon mean free path are reduced with increasing pressure. The secondary electron emission coefficient by the bombardment of ions with energies lower than 100 eV are small, e.g., typically from 10^{-2} to 10^{-1} under their experimental conditions. Therefore the contribution due to this process is negligible.

Several theoretical continuum models¹⁵⁻²⁸ have been developed for the application to the plasmas in the pressure range where the conditions of $\lambda_e \ll \lambda_D \ll R_p$ are fulfilled, where λ_e is the mean free path of electrons. Most of the theories mentioned above do not fulfill our experimental conditions except that of Su *et al.*²⁴ and Cohen.²⁵ Su *et al.* considered such cases where the electron density N_e is sufficiently high and where both ions and electrons make numerous collisions with the neutral particles before being collected by the probe. Under such conditions, they found that the sheath thickness became comparable to R_p for highly negative probe potentials and then calculated the probe characteristics for different D_λ . Cohen²⁵ used the same theoretical model as proposed by Su *et al.*,²⁴ assuming that λ_e and the ion mean free path λ_+ are shorter than the sheath thickness. All data points presented in this work fulfill this condi-

^{a)}Microstructure Research Center-fmt, University of Wuppertal, Rainer-Grüenter-Strasse 10, 42119 Wuppertal, Germany.

^{b)}Electronic mail: n2740908@ipc.shizuoka.ac.jp

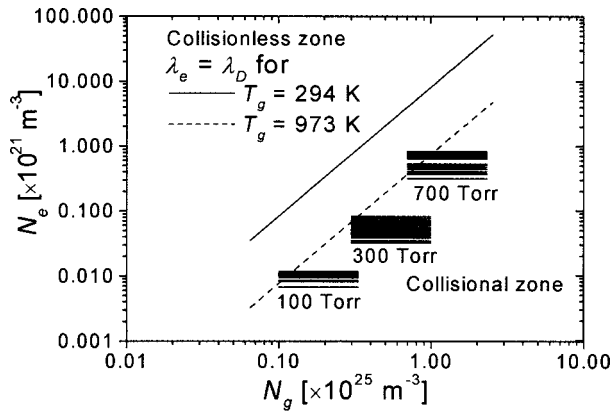


FIG. 1. Electron and neutral particle density ranges considered in this work. The lines indicate the collision-dominated sheath limit, where N_g and T_g are the neutral density and temperature, respectively.

tion, as shown in Fig. 1. Cohen presented numerically calculated probe characteristics in graphical form for the selected D_λ as a parameter. He found that the probe characteristics never saturate even at large V_p although they tend more nearly to saturate as D_λ becomes larger due to the influence of the probe potential which extends far beyond the space charge sheath. When the probe collects current, the probe potential decays only with D_λ^{-1} at a long distance from the probe. This indicates that the Debye shielding in the space charge sheath is incomplete. The expression of the results, however, is not convenient for the determination of electron temperature T_e from a practical probe characteristic. For this reason, the present work is aimed at developing a way that can provide the plasma parameters directly for any D_λ from 50 to 1600 and for any $\tau = T_+/T_e$ from 0 to 1 using discretized Cohen's results, where T_+ is the ion temperature.

II. HIGH PRESSURE PROBE THEORY

In this section the probe theory for high pressure plasma will be briefly reviewed for the sake of better understanding. When λ_e and λ_+ are much smaller than R_p , the motion of the particles can be described by the collision dominated processes of diffusion and drift. Su *et al.* considered a spherical probe in high density high pressure plasmas in the case that the probe is biased with a highly negative potential with respect to ϕ . In this case the Maxwell-Boltzmann distribution is assumed for electrons. Furthermore they considered the case of $\lambda_D < R_p$ and $T_+ < T_e$. They found that for small λ_D , the quasi-neutral solution breaks down near the probe surface, forming an ion sheath in front of the probe. In order to satisfy the condition of $N_e = N_+ = 0$ at the probe surface, a very thin ion diffusion layer should appear within the ion sheath when τ is small. Cohen assumed that the plasma density is sufficiently high and that ions and electrons make many collisions with the neutral particles before being collected by the probe, taking into account only elastic collisions, allowing one to use simplified continuity equations without source terms. But in reality many different processes can occur within the ion sheath, which cause the generation of ions. For example, collisions between two metastable helium atoms result in two-step processes in the production of

an ion and a fast electron. Conditions for which large current due to secondary electrons flows through the sheath, the direct impact ionization of neutrals, stepwise ionization of metastable species, or even three-body recombination of ions and electrons can be considered. But the contribution of these effects to the total ion flux at moderate negative potential of the probe is small as compared to the ion flux extracted from the bulk plasma. However, Cohen concentrated the analysis of the probe characteristics to the case of $V_p \ll \phi$. He solved the macroscopic particle flux equations by applying Einstein's relation together with Boltzmann's moment equations and Poisson's equation in order to determine the spatial profiles of N_e and ϕ , under the assumption that the diffusion coefficients $D_{e,+}$, mobility $\mu_{e,+}$ of electrons and ions, and $T_{e,+}$ are constant over the space and that λ_e and λ_+ are smaller than the sheath thickness.

Hereafter, the nondimensional probe potential φ_p is introduced for simplicity

$$\varphi_p = - \frac{e(\phi - V_p)}{\kappa T_e}, \tag{1}$$

where e and κ are the electronic charge and Boltzmann constant, respectively. One-dimensional solutions²⁴ of continuity equations and Poisson's equation for the spherical probe at $\varphi_p = 0$ are given by

$$N_e(r) = N_o \left(1 - \frac{I_e}{4\pi N_o e D_e} \frac{1}{r} \right), \tag{2a}$$

$$N_+(r) = N_o \left(1 - \frac{I_+}{4\pi N_o e D_+} \frac{1}{r} \right), \tag{2b}$$

where $D_{e,+}$ can be obtained as a function of T_e and T_+ from the data of gas discharges available in the literature by Brown²⁹ using the Einstein's relation

$$D_{e,+} = \frac{\kappa T_{e,+}}{e} \mu_{e,+}, \tag{3}$$

and I_e and I_+ are the electron and ion currents collected by the probe at $\varphi_p = 0$ and N_o is N_e and N_+ at $r = \infty$, i.e., $N_e(\infty) = N_+(\infty) = N_o$.

In Eq. (2a), I_e at $\varphi_p = 0$ should be equal to the random electron current I_{eR} . It is reasonable to assume $N_+ = N_e = 0$ at the probe surface. Therefore I_{eR} can be derived from Eq. (2a) as

$$I_{eR} = 4\pi R_p e N_o D_e \tag{4}$$

with

$$D_e = \frac{1}{3} \lambda_e v_{e,th}, \quad \lambda_e = \frac{1}{N_o \sigma_{c,e}}, \quad v_{e,th} = \sqrt{\frac{8\kappa T_e}{\pi m_e}}, \tag{5}$$

where $v_{e,th}$, m_e , and $\sigma_{c,e}$ are the thermal velocity, mass, and total collision cross section of electrons, respectively. The random electron flux per unit probe surface area Γ_{eR} can be written as

$$\Gamma_{eR} = \frac{I_{eR}}{4\pi R_p^2 e} = \frac{N_o v_{e,th}}{4} \left(\frac{4}{3} \frac{\lambda_e}{R_p} \right). \tag{6}$$

It should be noted that Γ_{eR} is reduced by a factor of $4\lambda_e/3R_p$ as compared to the case where collisions are absent in the sheath region.

Numerical results calculated by Cohen give the relations between I_e or I_+ and V_p in graphical form for the selected values of D_λ as a parameter. It is noted that the analytical formulas for the probe characteristics are not available in Cohen's analysis. However, to determine the plasma parameters from the measured probe characteristics, formulas expressing the probe characteristics for an arbitrary D_λ are required. In the present paper, we have developed a method which provides a set of algebraic formulas obtained by fitting the graphically presented results by Cohen with the modified Boltzmann function. From Eq. (6), I_{eR} is rewritten as

$$I_{eR} = eS\Gamma_{eR} = \frac{4}{3}\pi R_p e N_o \lambda_e \nu_{e,th}, \quad (7)$$

where $S = 4\pi R_p^2$ is the surface area of the spherical probe. The value of I_e for an arbitrary φ_p can be presumably expressed by introducing a function $I_{en}(\varphi_p, D_\lambda)$ as follows:

$$I_e = I_{eR} I_{en}(\varphi_p, D_\lambda). \quad (8)$$

Generally speaking, the probe current I_p consists of I_+ , I_e and the current I_{em} caused by the secondary electrons emitted from the probe. In high pressure high density plasmas, a large amount of secondary electrons³⁰ can be emitted from the probe due to the potential emission (Auger neutralization of ions or Auger deexcitation of metastable atoms). In such a case, I_p is modified to

$$I_p = I_e - I_+ - I_{em}. \quad (9)$$

With decreasing pressure, the contribution of I_{em} to I_p decreases because of increasing wall losses of metastable atoms. At pressures lower than 100 Torr, I_+ is already much higher than I_{em} . Therefore Eq. (9) reduces to

$$I_p = I_e - I_+. \quad (10)$$

In this case, $N_+(\infty)$ can be determined independently from $N_e(\infty)$ using the ion branch of the probe characteristics. For this purpose, an expression for I_+ is needed. Again the results of Cohen's analysis can be applied. The useful expressions to estimate $N_+(\infty)$ can be derived by the same procedure as that for electrons,

$$I_{+R} = 4\pi N_o e D_+ R_p = \frac{4}{3}\pi R_p e N_o \lambda_+ \nu_{+,th}, \quad (11)$$

$$\Gamma_{+R} = \frac{I_{+R}}{4\pi R_p^2 e} = \frac{N_o \nu_{+,th}}{4} \left(\frac{4}{3} \frac{\lambda_+}{R_p} \right), \quad (12)$$

with

$$D_+ = \frac{1}{3} \lambda_+ \nu_{+,th}, \quad \lambda_+ = \frac{1}{N_o \sigma_{c,+}}, \quad \nu_{+,th} = \sqrt{\frac{8\kappa T_+}{\pi m_+}}, \quad (13)$$

where I_{+R} and Γ_{+R} are the ion random current to the probe and the ion random flux per unit probe surface area and m_+ , $\sigma_{c,+}$, and $\nu_{+,th}$ are the mass, collision cross section, and thermal velocity of ions, respectively. Again Γ_{+R} is reduced by a factor of $4\lambda_+/3R_p$ as compared to the case of no collision in the sheath region.

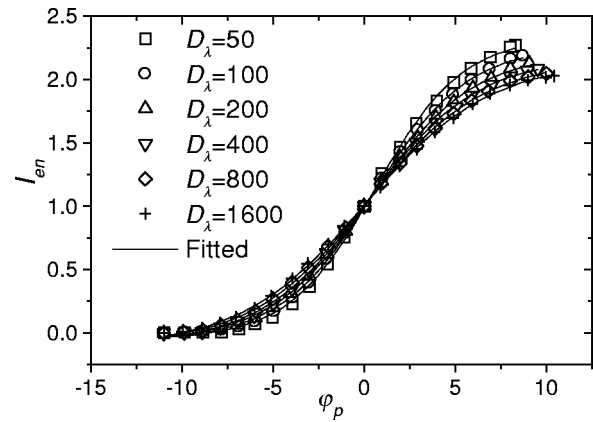


FIG. 2. Fitting of the normalized electron current I_{en} against the normalized probe potential φ_p for $\tau = 1.0$. Data shown by the marks have been collected from Ref. 26.

The ion current I_+ for an arbitrary φ_p is presumed as

$$I_+ = I_{+R} \tau^{-1} I_{+n}(\varphi_p, \tau, D_\lambda), \quad (14)$$

where $I_{+n}(\varphi_p, \tau, D_\lambda)$ is a function which should be determined based on Cohen's analysis.

III. DERIVATION OF ALGEBRAIC EQUATIONS

A. Electron current

As is well known, plasmas at high pressures can easily tend to thermal equilibrium state within a very short time after the onset of the discharge so that it is worthwhile to deduce $I_{en}(\varphi_p, D_\lambda)$ under the condition of $\tau = 1$. However, several methods to keep high pressure microwave or rf plasmas in nonthermal equilibrium state have been established since such plasmas are of great advantages to industrial uses. Therefore $I_{en}(\varphi_p, D_\lambda)$ is approximated for τ from 0 to 1 to analyze the probe characteristics measured in high pressure plasmas.

According to Cohen's calculation, the relation of I_{en} and φ_p does not depend on τ at all. At first, $I_{en}(\varphi_p, D_\lambda)$ is deduced using the numerical probe characteristics for $\tau = 1$ given by Cohen. It is assured to extend I_{en} for the values of τ different from 1. The marks in Fig. 2 show the relation between I_{en} and φ_p numerically calculated by Cohen under the condition of $\tau = 1$ for selected D_λ . In the present work an algebraic equation $I_{en}(\varphi_p, D_\lambda)$ best fitted to Cohen's results is deduced by modifying the Boltzmann function. After somewhat tedious considerations concerned with the dependence of I_{en} on φ_p , $I_{en}(\varphi_p, D_\lambda)$ is empirically presumed as

$$I_{en}(\varphi_p, D_\lambda) = \frac{A_1 \exp\left\{ \frac{\varphi_p - A_2(D_\lambda)}{A_3(D_\lambda)} \right\}}{1 + \exp\left\{ \frac{\varphi_p - A_2(D_\lambda)}{A_3(D_\lambda)} \right\}}. \quad (15)$$

Figure 2 shows that the solid curves calculated by Eq. (15) fit well with Cohen's data for each D_λ by adjusting the values of A_1 , A_2 , and A_3 for $\tau = 1$. Table I summarizes the dependence of A_1 , A_2 , and A_3 on D_λ . However, at the present situation, the values of A_1 , A_2 , and A_3 can be applied only for six values of D_λ used for fitting. In the practical use, A_1 ,

TABLE I. Dependence of A_1 , A_2 , and A_3 on D_λ for $\tau=1$.

D_λ	A_1	A_2	A_3
50	2.311 16	0.6857	2.228 86
100	2.229 47	0.583 65	2.391 33
200	2.165 97	0.476 41	2.533 89
400	2.1281	0.387 42	2.654 62
800	2.098 16	0.313 72	2.811 58
1600	2.084 58	0.251 89	2.958 14

A_2 , and A_3 should be given as a function of D_λ . Hence A_1 , A_2 , and A_3 can be approximated by the rational function of D_λ , respectively, as

$$A_1(D_\lambda) = \frac{2.551 + 4.165 \times 10^{-2} D_\lambda}{1 + 2.011 \times 10^{-2} D_\lambda}, \quad (16a)$$

$$A_2(D_\lambda) = \frac{0.835 + 1.29 \times 10^{-3} D_\lambda}{1 + 6.36 \times 10^{-3} D_\lambda}, \quad (16b)$$

and

$$A_3(D_\lambda) = \frac{2.104 + 1.107 \times 10^{-2} D_\lambda}{1 + 3.59 \times 10^{-3} D_\lambda}. \quad (16c)$$

For reference, the fitted curves of $A_1(D_\lambda)$, $A_2(D_\lambda)$, and $A_3(D_\lambda)$ are shown in Fig. 3. Using Eq. (15) along with Eq. (16), one can easily fit $I_{en}(\varphi_p, D_\lambda)$ to any D_λ from 50 to 1600.

B. Ion current

Contrary to I_{en} , I_{+n} given by Cohen strongly depends on τ so that the fitting equations are deduced with respect to τ from 0.001 to 1.0 for the convenience of probe data analysis. The dependence of $I_{+n}(\varphi_p, \tau, D_\lambda)$ on φ_p , τ , and D_λ given by Cohen's numerical results suggests the following fitting function based on the modified Boltzmann function. In this case, $I_{+n}(\varphi_p, \tau, D_\lambda)$ is made applicable not only to any D_λ from 50 to 1600 but to any τ from 0.001 to 1.0. In the way similar to $I_{en}(\varphi_p, D_\lambda)$, $I_{+n}(\varphi_p, \tau, D_\lambda)$ can be presumed empirically as

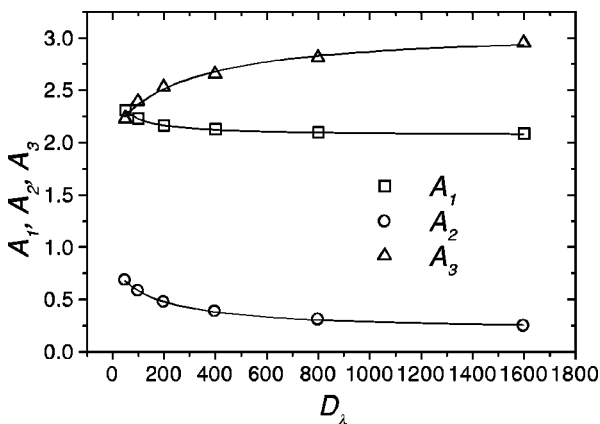


FIG. 3. Fitting of A_1 , A_2 , and A_3 to D_λ for $\tau=1.0$.

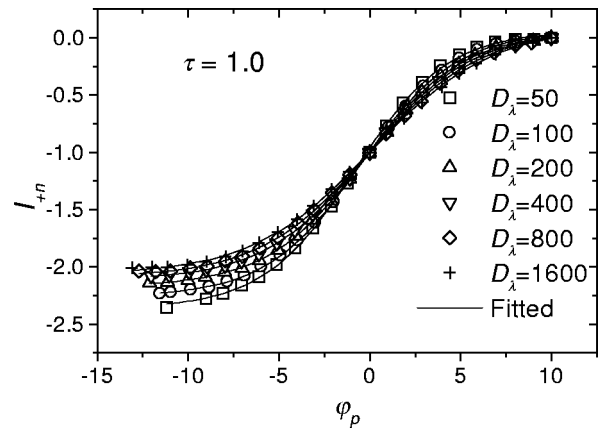


FIG. 4. Fitting of the normalized ion current I_{+n} against the normalized probe potential φ_p . Data shown by the marks have been collected from Ref. 26 for $\tau=1.0$.

$$I_{+n}(\varphi_p, \tau, D_\lambda) = \tau^{-1} \left[B_2(D_\lambda) C(\tau) + \frac{\{B_1(D_\lambda) - B_2(D_\lambda)\}}{1 + \exp\left(\frac{\varphi_p - B_3(D_\lambda)}{2.8368}\right)} \right]. \quad (17)$$

The symbols in Fig. 4 show Cohen's result for $\tau=1$ and the solid curves best fitted to the symbols. The parameters $B_1(D_\lambda)$, $B_2(D_\lambda)$, and $B_3(D_\lambda)$ are obtained in such a way that $I_{+n} - \varphi_p$ curves are best fitted to Cohen's numerical results and are summarized in Table II for different D_λ . Now $B_1(D_\lambda)$, $B_2(D_\lambda)$, and $B_3(D_\lambda)$ can be approximated by the following rational functions, respectively, as

$$B_1(D_\lambda) = \frac{-2.7092 - 27.08 \times 10^{-3} D_\lambda}{1 + 13.55 \times 10^{-3} D_\lambda}, \quad (18a)$$

$$B_2(D_\lambda) = \frac{0.1255 + 3.00 \times 10^{-4} D_\lambda}{1 + 2.29 \times 10^{-3} D_\lambda}, \quad (18b)$$

and

$$B_3(D_\lambda) = \frac{-4.9649 - 1.39 \times 10^{-3} D_\lambda}{1 + 10.124 \times 10^{-2} D_\lambda}. \quad (18c)$$

Figure 5 shows the curves for $B_1(D_\lambda)$, $B_2(D_\lambda)$, and $B_3(D_\lambda)$ for reference. Figure 6 shows Cohen's results at $D_\lambda=800$ for different τ by the symbols, together with the solid curves obtained using Eq. (17) in which $C(\tau)$ is adjusted to get best fitting. Table III summarizes the dependence of $C(\tau)$ on τ . However, at the present situation, Eq. (17) is applicable only

TABLE II. Dependence of B_1 , B_2 , and B_3 on D_λ for $\tau=1$.

D_λ	B_1	B_2	B_3
50	-2.424 89	0.112 66	-0.830 48
100	-2.294 96	0.099 27	-0.456 98
200	-2.190 45	0.0775	-0.256 64
400	-2.113 61	0.058 89	-0.1222
800	-2.067 54	0.038 79	-0.064 28
1600	-2.201 06	0.012 57	-0.056 58

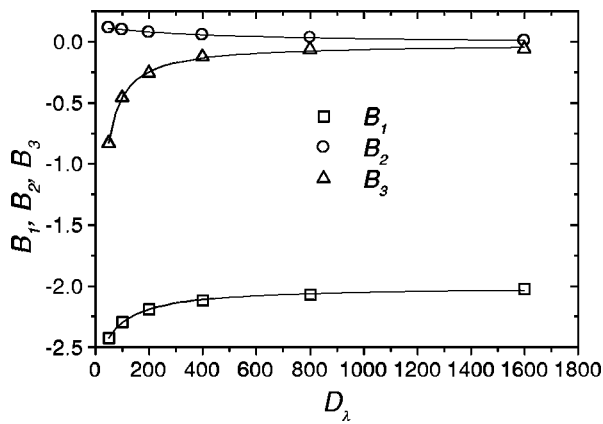


FIG. 5. Fitting of B_1 , B_2 , and B_3 to D_λ for $\tau=1.0$.

for eight values of τ . But for practical use, Eq. (17) should also be given as a function of τ . Hence $C(\tau)$ can be approximated by the following linear function as

$$C(\tau) = 28.47 - 28.164\tau. \tag{18d}$$

For example, the line best fitted to $C(\tau)$ is shown in Fig. 7. Now, using Eq. (17) along with Eq. (18), one can fit $I_{+n}(\phi_p, \tau, D_\lambda)$ for any D_λ from 50 to 1600 and for any τ from 0.001 to 1. It is noted that the curves shown in Fig. 5 do not fit well in the higher positive potential region. However, this region is not important under the present experimental conditions. Now, utilizing Eq. (14) together with Eq. (17) under the assumed conditions, one can analyze the probe characteristics obtained in high pressure plasmas.

C. Secondary electron emission from the probe surface

Generally, a probe can emit secondary electrons due to electron or ion impact, and photoemission or emission due to deexcitation of metastable atoms. When the probe is biased with highly negative potentials, emission by electron impact should be negligible. At high pressures when the probe diameter is relatively large,³¹ the secondary electron emission

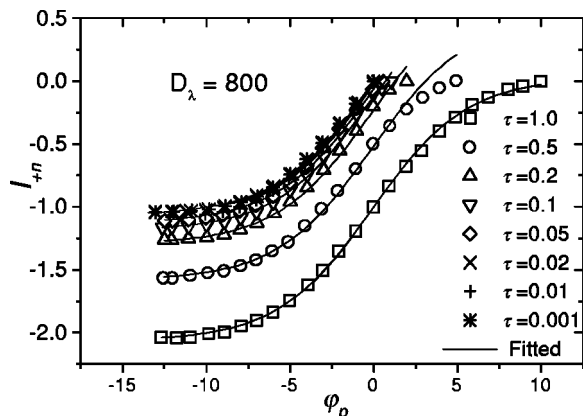


FIG. 6. Fitting of the normalized ion current I_{+n} against the normalized probe potential ϕ_p . Data shown by the marks have been collected from Ref. 26 for τ from 0.001 to 1.0 and $D_\lambda=800$.

TABLE III. Dependence of C on $\tau=T_+/T_e$.

$\tau=T_+/T_e$	C
1	0.872 24
0.5	13.489 02
0.2	22.359 68
0.1	25.333 45
0.05	26.970 74
0.02	28.440 93
0.01	28.587 27
0.001	28.729 48

current due ion impact can also be neglected because the emission current is two orders of magnitude higher than the thermal ion current.

The secondary electron emission current from the probe I_{em} was proposed by Kagan *et al.*¹⁴ under the influence of metastable atom fluxes to the probe given by

$$I_{em} = eS\gamma_m\Gamma_m = \frac{eN_{m0}S\gamma_m}{4} \sqrt{\frac{kT_m}{2\pi m_{He}}}, \tag{19}$$

where N_{m0} , T_m , and m_{He} are the density, temperature, and mass of metastable helium atoms, respectively; Γ_m is the metastable flux to the probe and γ_m is the secondary electron emission coefficient, which is of the order of 10^{-1} to 10^{-2} .¹⁴ With $T_m=973$ K, and $N_{m0}=7.6 \times 10^{21} \text{ m}^{-3}$, the estimated metastable flux is $4.3 \times 10^{24} \text{ m}^{-2} \text{ s}^{-1}$, which results in a current of 2 A emitted from the probe with a surface area of $3 \times 10^{-6} \text{ m}^2$. This value is two orders of magnitude higher than the actual ion currents in the probe characteristics, because Eq. (19) holds only for ion sheath thicknesses smaller than the mean free path of metastable particles. Taking a sheath thickness of 10^{-6} m , the limit of helium gas pressure for the applicability of Eq. (19) is about 12 Torr. So that at much higher pressures, a continuum model for a thin and a thick sheath should be considered.

1. Thin sheath approximation

At lower probe potential, the ion sheath is very thin and close to the probe surface and hence the sheath edge can be considered as the probe surface. Consequently, the metastable concentration at the probe surface is zero. Under the

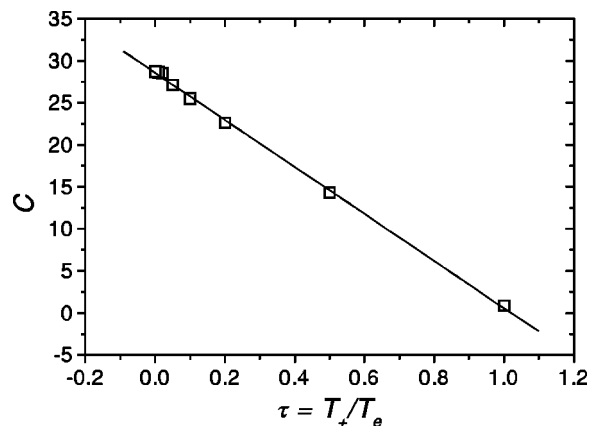


FIG. 7. Fitting of C against τ .

above conditions, the secondary electron emission current³² due to metastable atoms flux to the probe can be written as

$$I_{em} = -e \gamma_m S N_{m0} \sqrt{D_m N_o C_m}, \quad (20)$$

where D_m and C_m are the metastable diffusion coefficient and cumulative ionization rate coefficient, respectively. The thin sheath approximation can be used where the normalized probe potential is slightly negative or positive and gives the emission current which is independent of probe potential.

2. Thick sheath approximation

A thick sheath can be approximated by assuming that there are no free electrons and no production or destruction of metastables due to electron impact or stepwise ionization in the sheath region. Under these conditions, the metastable induced secondary electron emission current³² can be written as

$$I_{em} = -e \gamma_m S D_m \frac{N_{m0}}{\delta_{sh}}, \quad (21)$$

where δ_{sh} is the ion sheath thickness. δ_{sh} can be obtained by solving the one-dimensional Poisson's equation under the assumption of negligible electron density within the sheath and zero electric field at the sheath edge and can be written as

$$\delta_{sh} = \frac{3}{2} \left(\frac{1}{3} \lambda_e \lambda_D^2 \varphi_p^2 \right)^{1/3}. \quad (22)$$

The thick ion sheath approximation is applicable when (i) the ion sheath thickness is larger than the characteristic length of the metastable depletion zone; and (ii) the metastable density at the ion sheath edge can be regarded as equal to the density in the bulk plasma N_{m0} . This requirement means that the depletion of metastables at the sheath edge due to the metastable flux through the sheath is small, which is fulfilled for high electron density and consequently high production rate of metastables. The thick sheath model shows that the emission current depends on probe potentials.

3. Probe current with secondary electron emission

Considering our experimental conditions $P = 700$ Torr, $T_m = 973$ K, $D_m = 4.19 \times 10^{-4} \text{ m}^2 \text{ s}^{-1}$, $C_m = 1.14 \times 10^{-13} \text{ m}^3 \text{ s}^{-1}$, $N_{m0} = 7.6 \times 10^{21} \text{ m}^{-3}$, $\gamma_m = 10^{-1}$, and introducing the above values in Eqs. (11) and (20), it is found that $I_{+R} = 97.9 \text{ } \mu\text{A}$ and $I_{em} = 34.7 \text{ mA}$. So it is reasonable to consider that at high pressures, I_{em} is much larger than I_{+} . Therefore disregarding I_{+} with respect to I_{em} , Eq. (9) can be written as

$$I_p = I_{eR} I_{en}(\varphi_p, D_\lambda) - I_{em}. \quad (23)$$

Now one can easily apply Eq. (23) together with Eqs. (15) and (20) to analyze the probe characteristics measured in high pressure plasmas with high metastable density.

IV. MEASUREMENT OF THE PROBE CHARACTERISTICS IN HIGH PRESSURE MICROWAVE PLASMA

The probe characteristics are measured in high pressure microwave plasma. Figures 8–10 show the schematic diagram of the experimental setup developed to produce non-

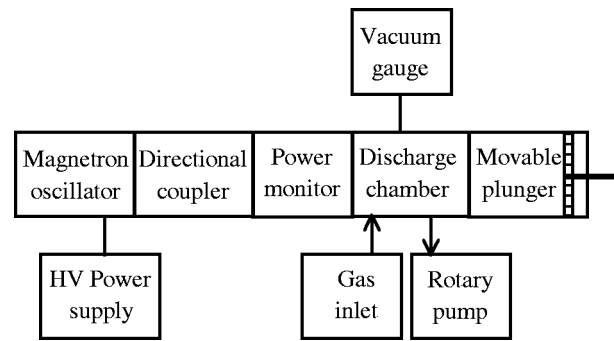


FIG. 8. Block diagram of the experimental setup.

thermal equilibrium plasmas, the cross-sectional view of the discharge chamber, the probe setup, respectively. The detailed description of the setup was published elsewhere.³ The discharge chamber is made of a rectangular waveguide 54 mm high, 108 mm wide, and 130 mm long. Open ends of the waveguide are closed by Pyrex glass plates in order to form the discharge chamber. Two cylindrical tungsten pipes of 4 and 6 mm in inner and outer diameters, respectively, are inserted perpendicularly through the H planes of the waveguide, as shown in Fig. 9. In order to study the radial profiles of N_e and T_e of the plasma, the probe is set up on the axis or at the edge of the plasma column as shown in Fig. 10. The spacing between the stub tips is maintained at 10 mm. In order to make a Langmuir probe, a tungsten wire of 0.8 mm in diameter embedded in insulation with an alumina tube is inserted through one of the stubs as shown in Fig. 10. The probe tip 1 mm long is placed at the center of the stub and along its axis. A 2.45 GHz pulsed microwave with a repetition frequency of 120 Hz is used for the plasma production. Helium is used as working gas.

Figure 11 shows the probe characteristics measured at helium pressures of 100, 300, and 700 Torr, respectively. It is found that I_p measured at 700 Torr has a dip at V_p from 0 to

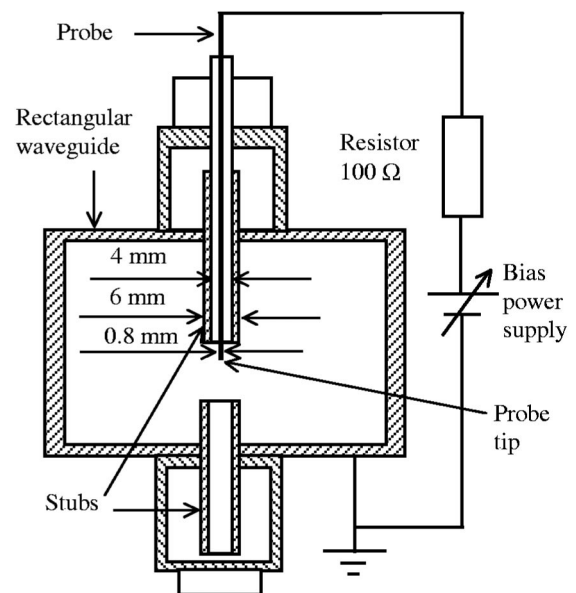


FIG. 9. Cross-sectional view of the discharge chamber.

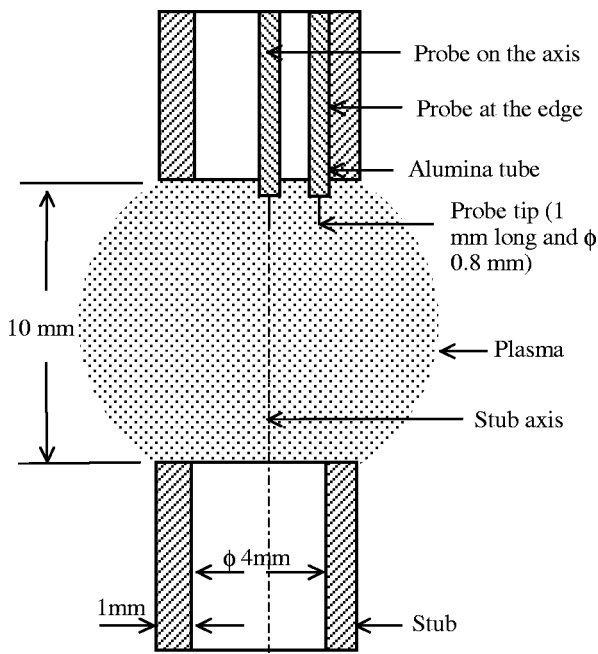


FIG. 10. The probe setup.

-40 V. The dip is caused by I_{em} , which is considered to be induced by the metastable helium atoms. The emissive probe theory³³ shows that at some conditions, a dip in the probe characteristics due to space charge effect can occur, looking similar to the curves as shown in Fig. 11. But the estimations for our experimental conditions show that this effect would occur for currents, which are orders of magnitude higher than the measured ones. On the other hand, for 100 and 300 Torr, the probe characteristics do not exhibit the remarkable secondary electron emission from the probe. The experimental probe characteristics suggest that the production rate of metastable helium atoms grows strongly with helium gas pressure. Thus I_{em} becomes predominant at 700 Torr.

V. ANALYSIS OF THE PROBE DATA

To obtain the plasma parameters, probe characteristics measured in high pressure microwave discharges have been

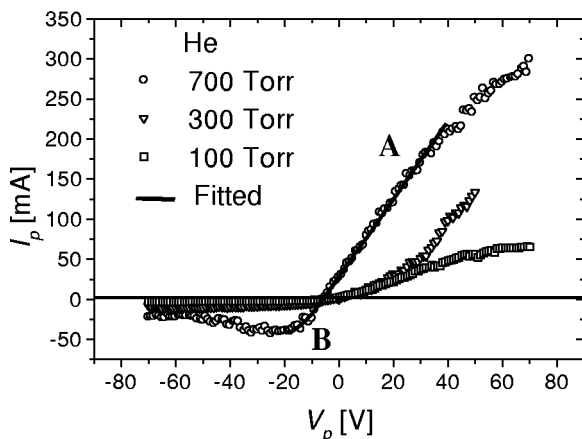


FIG. 11. Current–voltage probe characteristic at 0.80 ms after the starting of the microwave power pulse. A tungsten probe is used.

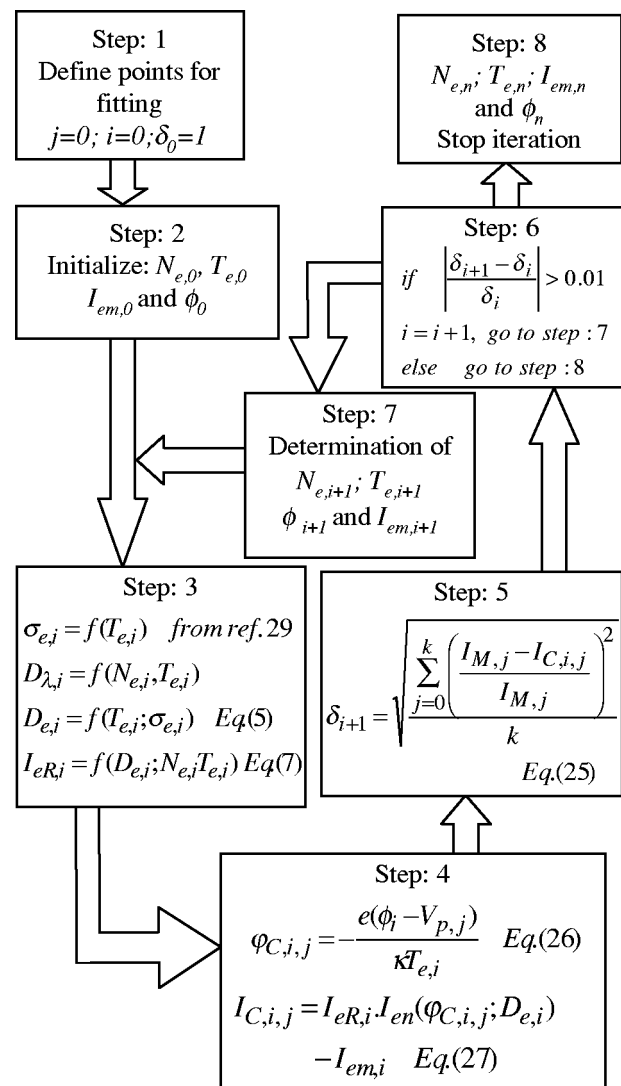


FIG. 12. Flow chart for the determination of plasma parameters.

fitted using an iterative procedure shown by a flow chart in Fig. 12. The best fitted curve can provide T_e , N_e , I_{em} , and ϕ . At first, the probe characteristic obtained at 700 Torr of helium shown in Fig. 11 is introduced for the estimation of plasma parameters. We have selected a portion for fitting from the whole probe characteristic in the following way. The point that the probe characteristic just starts bending gives the upper limit of the curve, as shown by point A in Fig. 11. The lower limit of the curve is chosen as the minimum probe current in the probe characteristic, as shown by point B in Fig. 11. In the estimation this minimum current is treated as I_{em} . Because of the increase in I_{em} at a pressure higher than 100 Torr, the ion part of the probe characteristic should not be adopted, otherwise it could provide overestimation of N_+ . The proposed fitting technique takes I_{em} into account and allows one to obtain reasonable plasma parameters even for strongly shifted probe characteristics due to secondary emission measured in atmospheric plasma.

The probe current I_p has been fitted using Eq. (23). The final value of N_e is calculated using the following equation:

$$N_e = \frac{I_{eR,n} + I_{em,n}}{4\pi R_p e D_{e,n}}, \quad (24)$$

where $I_{eR,n}$, $I_{em,n}$, and $D_{e,n}$ are the electron saturation current, the secondary electron emission current, and the diffusion coefficient obtained in the n th iteration, respectively. The relative error δ_i , used for the evaluation of fitting, is formulated for the probe current and is given by

$$\delta_{i+1} = \sqrt{\frac{\sum_{j=0}^k \left(\frac{I_{M,j} - I_{C,i,j}}{I_{M,j}} \right)^2}{k}}, \quad (25)$$

where $i=1,2,3,\dots,n$ is the number of iterations, $j=1,2,3,\dots,k$ is the number of measured points, $I_{M,j}$ is the measured probe current at the j th point, and $I_{C,i,j}$ is the probe current for the j th measured point calculated in the i th iteration, respectively. The iteration procedure shown in Fig. 12 for the determination of plasma parameters is described below.

Step 1: One has to define the following parameters. (a) The number of data points j to be considered will specify a portion from the whole probe characteristic for fitting. (b) The number of iterations i can be initialized by 0. (c) The estimated error δ_0 can be initialized as 1.

Step 2: The values of N_e , T_e , I_{em} , and ϕ can be initialized by assumption. If these initialized values are very close to the calculated ones, even a few iterations can provide the best fitting. Otherwise, the number of iterations will be increased to get the best fitting.

Step 3: The value of σ_e can be found from Ref. 29. The values of D_e and I_{eR} can be determined using Eqs. (5) and (7), respectively.

Step 4: The values of φ_p and I_p in the iteration process can be calculated by using Eqs. (1) and (23), respectively. These two equations can be written as

$$\varphi_{C,i,j} = - \frac{e(\phi_i - V_{p,j})}{\kappa T_{e,i}} \quad (26)$$

and

$$I_{C,i,j} = I_{eR,i} I_{en}(\varphi_{C,i,j}; D_{e,i}) - I_{em,i}, \quad (27)$$

where $\varphi_{C,i,j}$ is the normalized probe potential at the j th measured point in the i th iteration, $V_{p,j}$ is the probe potential at the j th point, ϕ_i , $T_{e,i}$, $I_{eR,i}$, $D_{e,i}$, and $I_{em,i}$ are the space potential, the electron temperature, the random electron current, the electron diffusion coefficient, and the secondary electron emission current in the i th iteration, respectively.

Step 5: Relative error δ_i is estimated using Eq. (25).

Step 6: Compare δ_i and δ_{i+1} . If $|(\delta_{i+1} - \delta_i)/\delta_i| > 0.01$, the next iteration will be started by taking the new values of N_e , T_e , I_{em} , and ϕ .

Step 7: If $|(\delta_{i+1} - \delta_i)/\delta_i| \leq 0.01$, the iteration will be finished and the best fitted curve will provide the plasma parameters N_e , T_e , I_{em} , and ϕ . An example of the best fitted curve for 700 Torr is shown by the solid curve in Fig. 11.

The ion current I_+ has been fitted for 100 Torr using Eq. (14) by an analogous procedure as that of the electron current fitting. In this case, the values of T_e and ϕ are used which

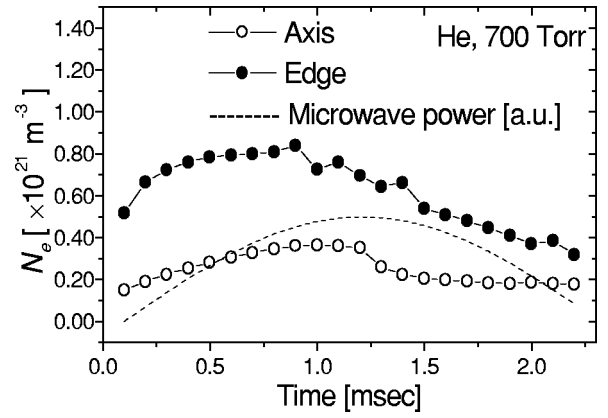


FIG. 13. Temporal development of electron density in a helium discharge at 700 Torr after the starting of the microwave power pulse.

were obtained from the electron current fitting. The value of T_+ can be calculated neglecting I_{em} , considering $N_e = N_+ = N_o$ and using the following equation:

$$T_+ = \frac{4\pi R_p N_+ e \lambda + \nu_{+,th} T_e}{3I_{+,R,n}}, \quad (28)$$

where $I_{+,R,n}$ is the final value of $I_{+,R}$ obtained by fitting.

VI. RESULT AND DISCUSSION

In order to investigate the transient behavior of atmospheric microwave discharge plasmas, microwave power pulses of 400 W with a repetition frequency of 120 Hz have been applied to the discharge chamber. The probe characteristic data have been recorded by a digital oscilloscope. The step between the consecutive probe voltages has been maintained at 1 V. In order to reduce noise of the probe current, the probe current has been recorded after averaging over 300 microwave pulses.

Figure 13 shows the temporal development of N_e both on the axis and at the edge of the plasma column for 700 Torr together with the microwave pulse. When the probe is placed at the edge of the plasma column, N_e increases with time and reaches a maximum of $8.40 \times 10^{20} \text{ m}^{-3}$ at 0.90 ms. This increase in N_e is due to the microwave heating. After 0.90 ms N_e starts to decrease together with the microwave pulse and monotonically decreases up to 2.20 ms. This temporal development of N_e is similar in appearance to that of spectroscopic measurements by Vikharev⁵ at 750 Torr for a helium plasma. On the other hand, when the probe is positioned on the axis of the plasma column, N_e increases more slowly and reaches a maximum of $3.65 \times 10^{20} \text{ m}^{-3}$ at 1.00 ms. This increase in N_e is considered responsible for microwave heating and diffusion from the edge of the plasma column. Then N_e starts to decrease after 1.20 ms. The following reasons may be responsible for the difference of N_e measured at two points: at the beginning of the discharge, the microwave can easily penetrate into the plasma column because N_e is lower than the critical density N_c of $7.4 \times 10^{16} \text{ m}^{-3}$. Just after the onset of the discharge, N_e exceeds N_c , which consequently reduces the microwave power inside the plasma column. After 1.20 ms, the microwave is confined near the surface of

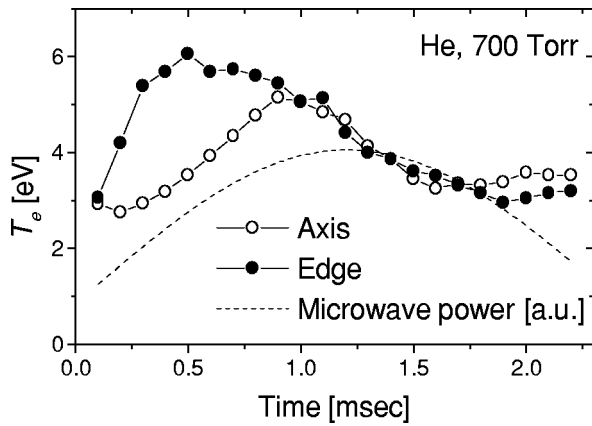


FIG. 14. Temporal development of electron temperature in a helium discharge at 700 Torr after the starting of the microwave power pulse.

the plasma column. However, the microwave power penetrating into the plasma reduced by skin effect is still intense enough to produce the plasma. In addition, the ambipolar diffusion of the plasma near the plasma column surface raises the plasma density on the axis of the plasma column. As a result, N_e reduces and remains relatively constant at the center of the plasma column.

Temporal development of T_e measured at the edge and on the axis of the plasma column is shown in Fig. 14. When the probe is placed at the edge, T_e increases sharply with time from the beginning of the discharge up to 6.07 eV at 0.50 ms due to microwave heating. After 0.70 ms, T_e starts to decrease up to 1.90 ms and then seems to be constant. On the other hand, T_e on the axis of the plasma column is lower than that at the edge at the beginning of the discharge, increases linearly with increasing time, and reaches the maximum of 5.15 eV at 0.90 ms. After 0.90 ms, it starts to decrease continuously up to 1.60 ms and then T_e becomes almost constant.

Profiles of N_e and T_e measured here may be caused by the following effects. The plasma with densities higher than N_c is mainly produced inside a thin layer near the plasma column surface. Therefore the plasma on the axis of the plasma column should be kept intact by plasma particles diffusion from the plasma production layer and the ionization due to the microwave power penetrating through the skin effect enlarged layer due to high electron-neutral collisions. The high energy electrons on the surface of the plasma column can diffuse toward the center of the discharge so that T_e increases. The skin depth estimated under the present condition is around 5.6 mm which results in an effective penetra-

tion of microwave power into the plasma. Therefore it is reasonable to consider that the plasma can be produced or heated by the reduced microwave power even near the plasma axis, though N_e and T_e at the edge are higher than those near the axis because of the higher microwave power dissipation.

The pressure dependence T_e and N_e at the edge and on the axis of the plasma column are compared in Table IV. It can be seen that T_e at 300 Torr is lower than that at 100 Torr because the number of collisions of electrons with neutral particles increases with increasing pressure and hence the electrons lose their energy. But T_e at 700 Torr is comparatively higher because of the presence of high energy electrons in the vicinity of the probe, as explained below. On the other hand, N_e increases with increasing pressure. In most cases it is found that N_e is higher at the edge than that on the axis.

It has been mentioned earlier that the emission of secondary electrons is caused by potential emission-like Auger neutralization and deexcitation due to ions and excited atoms on the probe surface. The energy of the secondary electrons due to Auger neutralization of ions at the metal surface can be evaluated.³⁰ The maximum energy of the secondary electrons $E_{i,max}$ is given by $E_{i,max} = E_i - 2W$, where E_i is the ionization energy of the atoms and W is the work function of the metal. For the combination of helium and tungsten, $E_{i,max} = 15.58$ eV, where $E_i = 24.58$ eV and $W = 4.5$ eV are used. The maximum energy of the emitted electrons due to the Auger deexcitation by the excited atoms at the tungsten surface $E_{ex,max}$ corresponds to 15.31 eV, since $E_{ex,max} = E_{ex} - W$, where $E_{ex} = 19.81$ eV is the excitation energy of helium. Therefore the secondary electrons have higher energy than most electrons in the bulk plasma, which leads to higher T_e as shown in Table IV. This anomaly can also be explained in terms of the influence of the metastable atoms on the electron energy distributions.³⁴ The role of wall losses on the balance of metastables decreases with increasing pressure and consequently higher metastable density can be expected. One of the main loss mechanisms is the collision between two metastables, leading in consequence to ionization of one, deexcitation of the other metastable, and releasing of the high energy electron. Because the density of metastable atoms is orders of magnitude higher than the electron density, this mechanism can have a strong impact on the electron energy distribution, contributing to its high-energy tail. By assuming a Maxwell-Boltzmann electron energy distribution function, such a tail is leading to higher measured electron temperatures.

TABLE IV. Electron density and temperature measured on the axis and at the edge of the plasma column at 2.00 ms after the onset of the discharge as a function of the helium pressure.

Pressure (Torr) <i>P</i>	Electron temperature T_e (eV)		Electron density N_e (m^{-3})	
	Axis	Edge	Axis	Edge
100	2.65	3.15	1.29×10^{19}	8.61×10^{18}
300	1.92	2.77	2.76×10^{19}	3.48×10^{19}
700	3.59	3.06	1.88×10^{20}	3.71×10^{20}

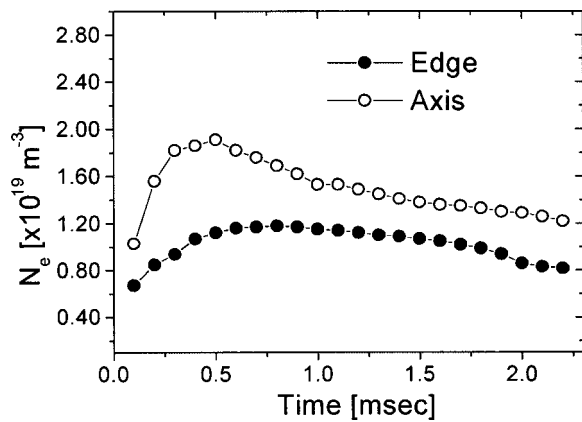


FIG. 15. Temporal development of electron density in a helium discharge at 100 Torr after the starting of the microwave power pulse.

The temporal development of N_e and temperatures for 100 Torr are shown in Figs. 15 and 16, respectively. N_e curves for 100 Torr show an inverse relation as compared to that for 300 Torr (Table IV) and 700 Torr (Fig. 13). N_e at the axis is higher than that at the edge during the entire cycle time for 100 Torr. This can be explained by the increase of D_e with decreasing pressure. Even though the production of electrons is concentrated in the ring-shaped zone between the two tubular electrodes, overlapping of the diffusion zones at the axis may cause a maximum at this position.

Finally, the relation of R_p and λ_e or λ_+ and λ_D is evaluated to justify the applicability of the probe theory. It can be seen from Fig. 1 that almost all data fall within the collision-dominated zone for 100, 300, and 700 Torr, which can completely fulfill the assumption of the present probe theory.

The high pressure microwave discharge produced by the present discharge chamber can produce nonthermal plasmas, since helium gas causes a rapid cooling of ionized and neutral atoms because of their small mass. Moreover, the interaction of helium ions with the stub wall can extract energy

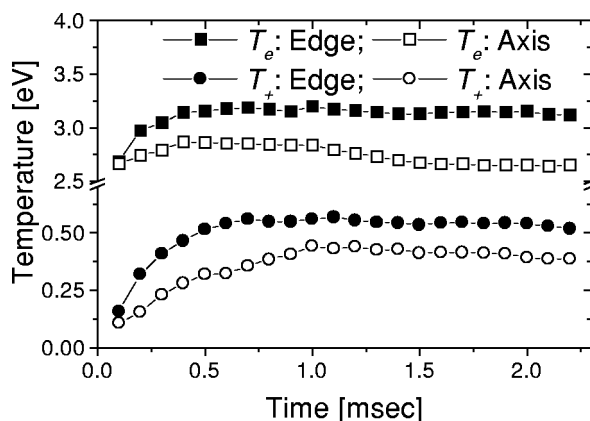


FIG. 16. Temporal development of electron and ion temperatures in a helium discharge at 100 Torr after the starting of the microwave power pulse.

from helium ions effectively. Consequently, nonthermal equilibrium will take place within a very short time.

VII. SUMMARY

A method for the determination of T_e and N_e is proposed using numerical results of the continuum model by Cohen. Simple algebraic functions provide the basis for using iterative procedures for the determination of plasma parameters avoiding making the fitting parameters discrete. The proposed fitting technique takes the secondary electron current due to metastable excited atoms induced emission into account and allows one to obtain reasonable plasma parameters even if the secondary electron emission current strongly affects the probe characteristics. Fitting of the ion saturation current is used to estimate T_+ , provided that T_e and N_e are known. The present method was applied to high pressure high density microwave discharges using a moderate microwave power of 400 W.

- ¹J. Park, I. Henins, H. W. Herrmann, G. S. Selwyn, J. Y. Jeong, R. F. Hicks, D. Shim, and C. S. Chang, *Appl. Phys. Lett.* **76**, 288 (2000).
- ²O. A. Ivanov, A. M. Gorbachev, V. A. Koldanov, A. L. Kolisko, and A. L. Vikharev, *J. Phys. IV* **8**, 317 (1998).
- ³M. Kando, *Eleventh Symposium on Elementary Processes and Chemical Reactions in Low Temperature Plasma* (Low Tatras, Slovakia, 1998), p. 73.
- ⁴M. R. Talukder, D. Korzec, and M. Kando, in *Proceedings of the XXV International Conference on Phenomena in Ionized Gases*, edited by T. Goto (Nagoya University, Nagoya, Japan, 2001), Vol. 4, p. 271.
- ⁵A. L. Vikharev, *J. Phys. IV* **8**, 275 (1998).
- ⁶J. F. Waymouth, *Phys. Fluids* **7**, 1843 (1964).
- ⁷G. K. Bienkowski and K. W. Chang, *Phys. Fluids* **11**, 784 (1968).
- ⁸Y. S. Chou, L. Talbot, and D. R. Willis, *Phys. Fluids* **9**, 2150 (1966).
- ⁹V. M. Zakharova, Yu. M. Kagan, K. S. Mustafin, and V. I. Perel, *Sov. Phys. Tech. Phys.* **5**, 411 (1960).
- ¹⁰E. Wasserstrom, C. H. Su, and R. F. Probstein, *Phys. Fluids* **8**, 56 (1965).
- ¹¹Z. Zakrzewski and T. Kopiczynski, *Plasma Phys.* **16**, 1195 (1974).
- ¹²G. L. Schulz and S. C. Brown, *Phys. Rev.* **98**, 1642 (1955).
- ¹³R. L. F. Boyd, *Proc. R. Soc. London* **64B**, 795 (1951).
- ¹⁴Yu. M. Kagan and V. I. Perel, *Sov. Phys. Usp.* **6**, 767 (1964).
- ¹⁵M. B. Hopkins and W. G. Graham, *Rev. Sci. Instrum.* **57**, 2210 (1986).
- ¹⁶P. R. Smy, *Adv. Phys.* **25**, 517 (1976).
- ¹⁷E. Leveroni and E. Pfender, *Rev. Sci. Instrum.* **60**, 3744 (1989).
- ¹⁸W. B. Bush and F. E. Fendell, *J. Plasma Phys.* **4**, 317 (1970).
- ¹⁹K. Toba and S. Sayano, *J. Plasma Phys.* **1**, 407 (1967).
- ²⁰F. Fendell, *Combust. Sci. Technol.* **1**, 331 (1970).
- ²¹R. L. Chapkis and E. Baum, *AIAA J.* **9**, 1963 (1971).
- ²²J. S. Chang and J. G. Laframboise, *Phys. Fluids* **19**, 25 (1976).
- ²³M. S. Benilov, *J. Phys. D* **33**, 1683 (2000).
- ²⁴C. H. Su and S. H. Lam, *Phys. Fluids* **6**, 1479 (1963).
- ²⁵I. M. Cohen, *Phys. Fluids* **6**, 1492 (1963).
- ²⁶J. D. Swift and M. J. R. Schwar, *Electrical Probes for Plasma Diagnostics* (Illifee, London, 1970), Chap. 4, pp. 113–200.
- ²⁷F. F. Chen, *Plasma Diagnostic Technique*, edited by R. H. Huddleston and S. L. Leonard, (Academic, New York, 1965), Chaps. 9 and 10, pp. 172–219.
- ²⁸P. M. Chung, L. Talbot, and K. J. Touryan, *Electric Probes in Stationary and Flowing Plasmas* (Springer-Verlag, Berlin, 1975).
- ²⁹S. C. Brown, *Basic Data of Plasma Physics*, 1966, 2nd ed. (MIT, Cambridge, MA, 1966), Chap. 4, pp. 79–129.
- ³⁰H. D. Hagstrum, *Phys. Rev.* **96**, 336 (1954).
- ³¹S. Klage and M. Tichu, *Czech. J. Phys., Sect. B* **35**, 988 (1985).
- ³²D. Korzec, M. R. Talukder, and M. Kando, *Sci. Technol. Adv. Mater. (STAM)* **2/3-4**, 595 (2001).
- ³³K. W. Chang and G. K. Bienkowski, *Phys. Fluids* **13**, 902 (1970).
- ³⁴L. J. Overzet and J. Kleber, *Plasma Sources Sci. Technol.* **7**, 512 (1998).